Supplement of Earth Syst. Sci. Data, 18, 465–491, 2026
https://doi.org/10.5194/essd-18-465-2026-supplement

Open Access Earth System Science Data

Supplement of

CN_Wheat10: a 10 m resolution dataset of spring and winter wheat distribution in China (2018–2024) derived from time-series remote sensing

Man Liu et al.

Correspondence to: Hongyan Zhang (zhanghongyan@cug.edu.cn)

Table S1: Details of the spectral indices used in this study.

Index	Full name	Formula	References
EVI	Enhanced vegetation index	(B8-B4) / (B8+6*B4-7.5*B2+1)	(Huete et al., 2002)
GCVI	Green chlorophyll vegetation index	B8 / B3-1	(Gitelson et al., 2003)
GNDVI	Green normalized difference vegetation index	(B8-B3) / (B8+B3)	(Gitelson et al., 1996)
LSWI	Land surface water index	(B8-B11) / (B8+B11)	(Xiao et al., 2006)
NDVI	Normalized difference vegetation index	(B8-B4) / (B8+B4)	(Huete et al., 2002)
NDWI	Normalized difference water index	(B3-B8) / (B3+B8)	(Gao, 1996)
NDYI	Normalized Difference Yellowness Index	(B3-B2) / (B3+B2)	(Sulik and Long, 2016)
NREDI1	Normalized red edge1 difference vegetation index	(B6-B5) / (B6+B5)	
NREDI2	Normalized red edge2 difference vegetation index	(B7-B5) / (B7+B5)	(Gitelson and Merzlyak, 1994)
NREDI3	Normalized red edge3 difference vegetation index	(B7-B6) / (B7+B6)	
OSAVI	Optimized soil adjusted vegetation index	1.5*(B8-B4) / (B8+B4+0.16)	(Rondeaux et al., 1996)
PSRI	Plant senescence reflectance index	(B4-B3) / B8	(Fernández-Manso et al., 2016)
RVI	Ratio Vegetation Index	B8 / B4	(Jordan, 1969)
SWI	Shade water index	B2+B3-B8	(Li et al., 2016)
WRI	Winter rapeseed index	B2*(B8-B3) / ((B8+B3)*(B4+B3))	(Zhang et al., 2022)

S1: The details of the sample point data

Approximately 2,000–3,000 points were collected from field surveys each year during 2020–2024. These field samples were mainly distributed in the Huang-Huai-Hai Plain and the middle and lower reaches of the Yangtze River Plain, with smaller numbers in other provinces. The spatial distribution of the field survey samples is illustrated in Fig.S1.

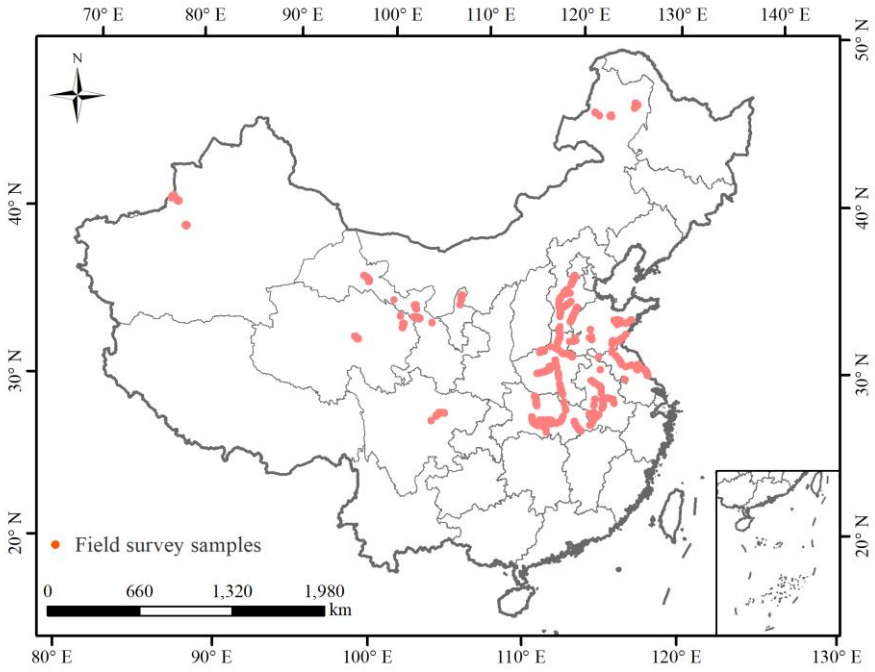

Figure S1: Spatial distribution of sample points from field surveys in 2020-2024.

In the process of visual interpretation of remote sensing images, wheat is distinguished from other crop types mainly based on three criteria, taking winter wheat as an example: (1) Temporal dynamics (Fig.S2(a)): multi-temporal imagery from October to the following June reveals the complete growth cycle of winter wheat, including sowing, overwintering, regreening, jointing, heading, grain filling, and maturity, while other crops exhibit distinct temporal profiles; (2) Spectral characteristics (Fig.S2(b)): winter wheat demonstrates high vegetation indices during the mid-growing season (around April), appearing as dark green in imagery, whereas rapeseed typically appears yellow and garlic is often light green; (3) Texture and spatial distribution (Fig.S2(b)): winter wheat fields are generally regular in shape and spatially aggregated, in contrast to other land cover types, which often appear fragmented or irregular.

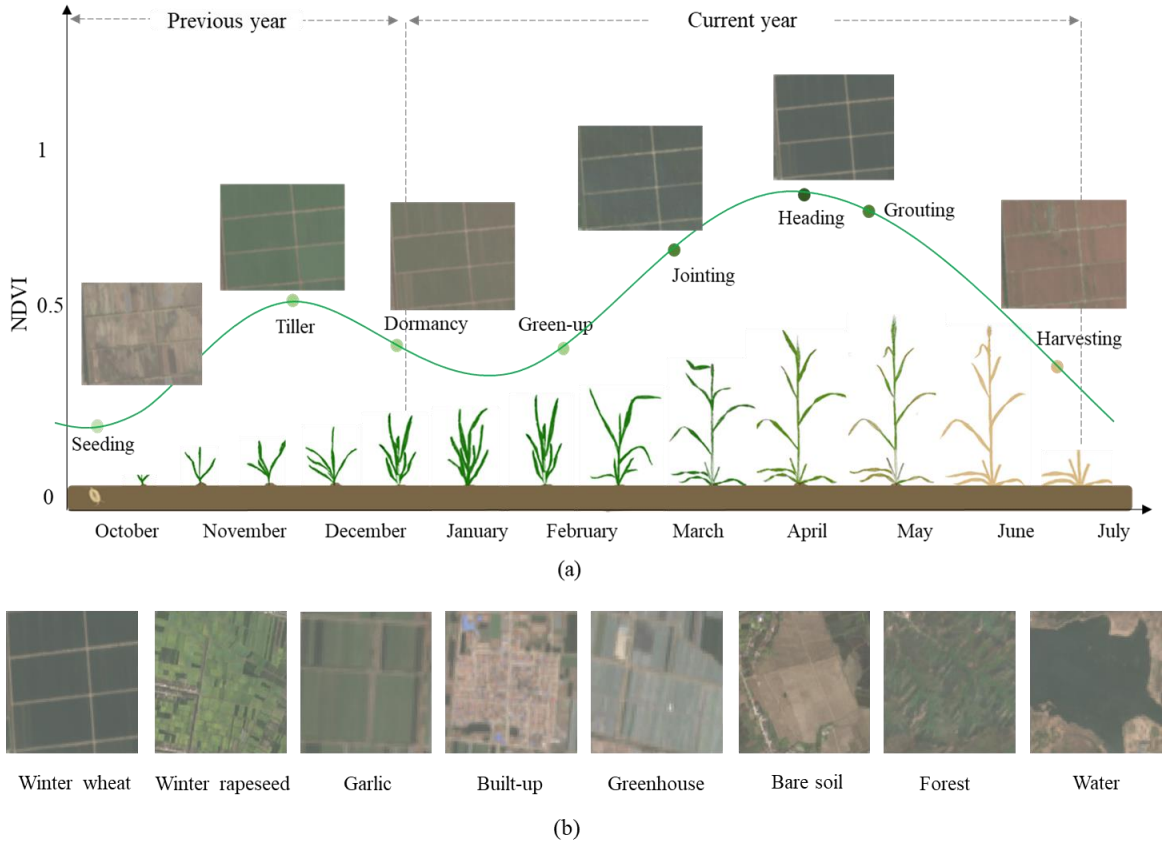

Figure S2: Distinguishing winter wheat from other land-cover types based on visual interpretation from Sentinel-2 images. (a) Phenological spectrum curve of winter wheat and remote sensing image characteristics at different growth stages. (b) Spectral texture characteristics of winter wheat and other land-cover types in April.

As shown in Fig.S3, we take Xinyang City in Henan Province as an example to demonstrate the spatial hierarchical sampling strategy based on quadrilateral grids. We first divided the study area into a series of regular quadrilateral grids within the Google Earth Engine platform and examined the monthly Sentinel-2 composite imagery from October to the following June. During the interpretation process, all land cover types were classified into six categories: winter wheat, built-up, water, trees, bare land, and other crops. Based on the proportional coverage of each land cover type within a grid, no more than 10 sample points were randomly selected per grid, thereby avoiding excessive spatial clustering of samples. Specifically, for grids containing wheat fields, 1–8 wheat samples were randomly selected in proportion to the wheat coverage within the grid, along with additional non-wheat samples to maintain category balance. For grids without wheat fields, 1–2 non-wheat samples were randomly selected for each category, including built-up land, trees, water bodies, and bare land. This approach ensured both the spatially uniform distribution of samples and the representativeness of diverse land cover types.

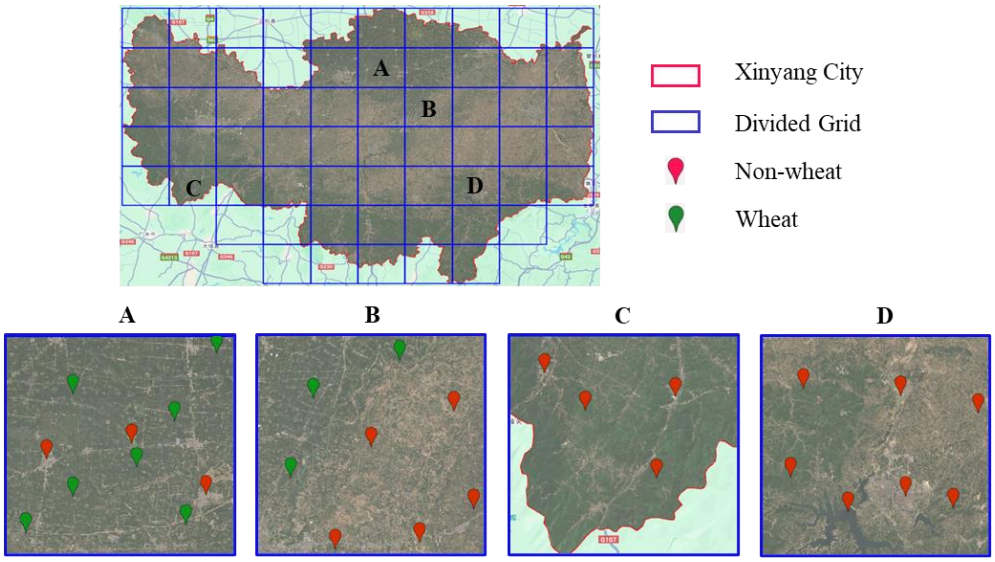

Figure S3: Spatial stratified sampling strategy in Xinyang City based on Sentinel-2 imagery processed in Google Earth Engine. Imagery © 2024 ESA, Map data © 2025 Google.

Table S2: Distribution of wheat verification points in each province.

	2018 (VI)		2019 (VI)		2020 (FS+VI)		2021 (FS+VI)		2022 (FS+VI)		2023 (FS+VI)		2024 (FS+VI)	
	wheat	non-wheat	wheat	non-wheat	wheat	non-wheat	wheat	non-wheat	wheat	non-wheat	wheat	non-wheat	wheat	non-wheat
AH	467	1503	533	1486	2024	3275	1175	5042	602	1944	334	2344	555	3479
HB	512	1967	458	2099	1595	2881	1362	2436	877	2260	685	2253	466	2121
HN	726	3586	668	3000	1581	5752	1158	4630	907	3570	836	3581	713	3447
HuB	477	2329	372	2004	605	2663	466	2675	422	2690	458	765	438	3173
JS	522	2243	451	2119	1425	3877	597	2746	692	2291	479	2076	538	2243
SD	722	3324	616	3263	2421	5658	1196	4227	978	3330	738	3209	700	3335
SX	544	1828	337	1782	583	2789	782	2157	309	1952	247	1672	306	1754
SAX	461	1981	566	2073	196	1879	608	2596	500	1774	488	1770	359	1942
SC	301	2683	326	2812	786	3768	314	3368	309	2921	218	2552	311	2717
ZJ	261	1493	252	1491	980	1725	179	1689	422	1668	387	1415	390	1597
XJ	1161	5423	1054	5438	807	5161	1017	5331	1050	5412	802	5259	887	5221
GS	713	5500	786	5440	1234	5223	710	5776	975	6832	799	6729	707	7226
NM	555	4959	514	4860	782	3753	436	4325	403	4667	738	5902	655	4694
QH	353	3108	452	3123	529	2806	412	3042	301	2826	363	3306	445	3328
NX	427	2804	499	2834	385	3013	443	2739	518	2779	464	2694	435	2821
Total	52933		51708		70156		63634		56181		53563		57003	

Note: FS refers to verification data obtained from field survey, VI refers to verification data obtained from visual interpretation of high-resolution images

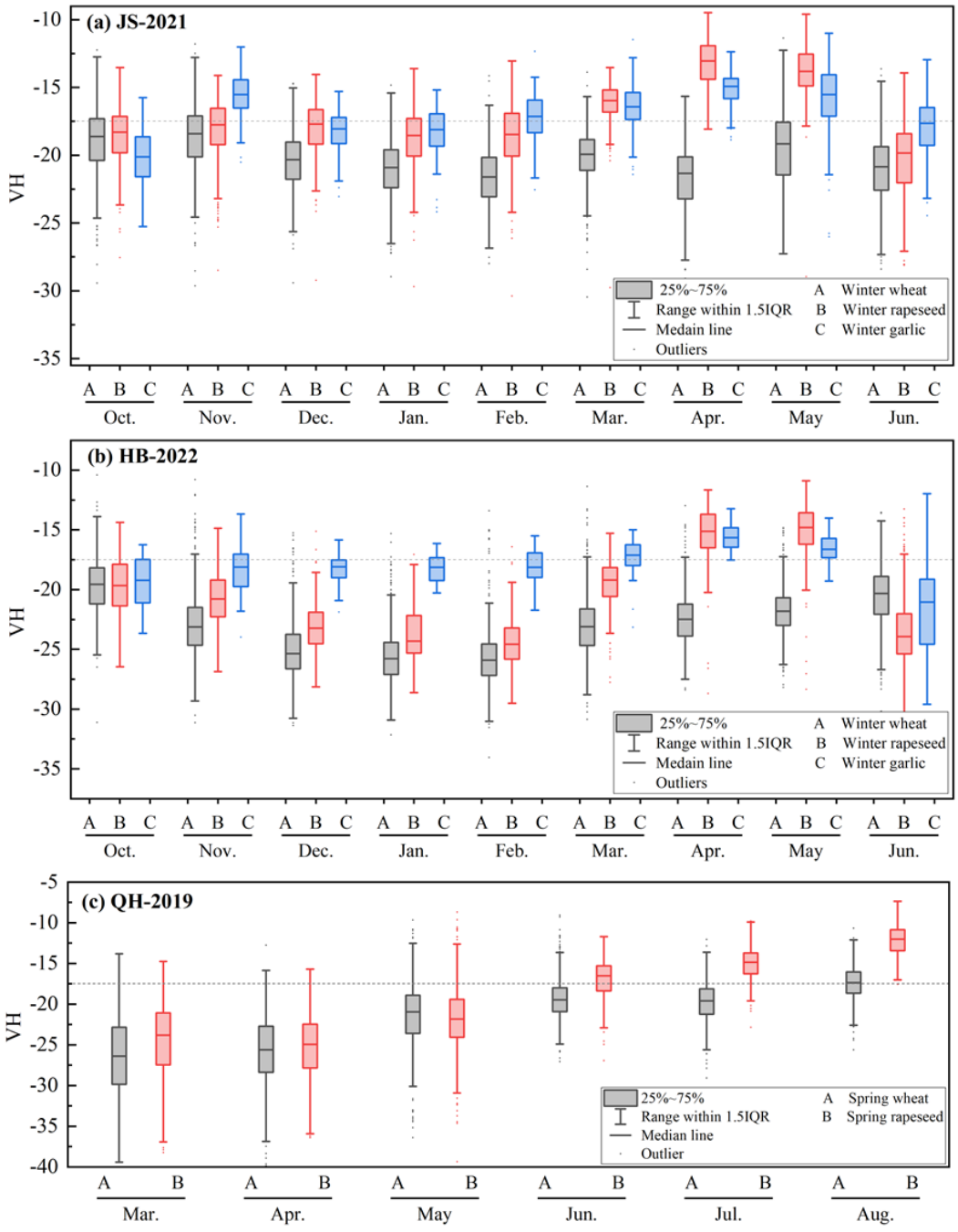

Figure S4. Distribution of VH backscatter values of different crops in Jiangsu Province (2021), Hebei Province (2022) and Qinghai Province (2019).

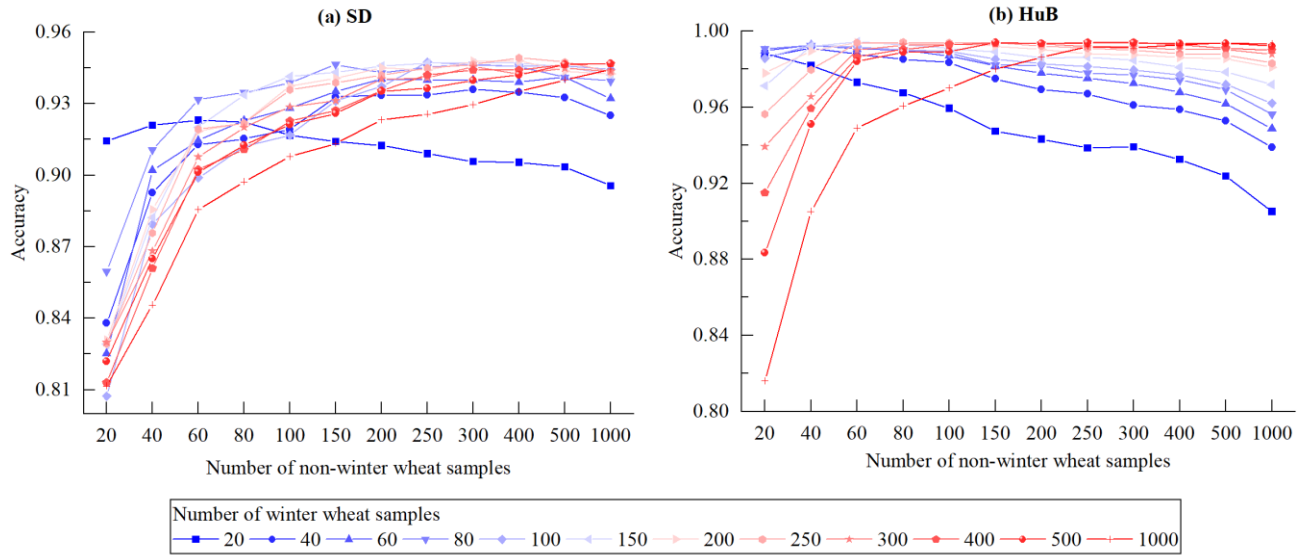

Figure S5. Changes in accuracy of winter wheat mapping under different sample sizes. (a)Variation trend of wheat accuracy in Shandong (SD) province. (b)Variation trend of wheat accuracy in Hubei (HuB) province.

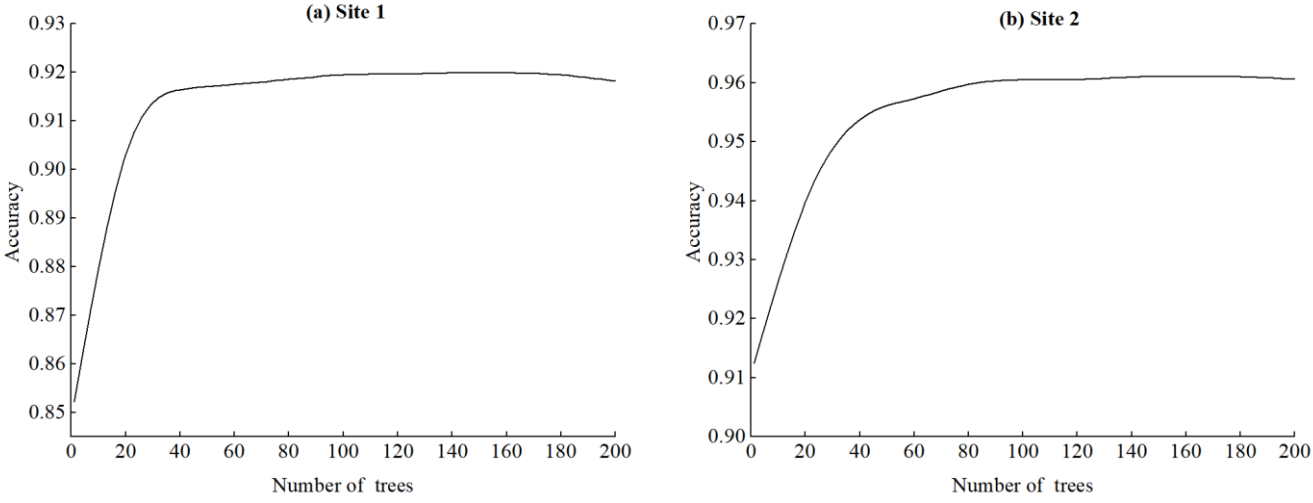

Figure S6. Trends in accuracy of RF classifiers under different parameters at two study sites.

Table S3: Top five features with highest frequency in each province.

Provinces	The top five features with the highest frequency
AH	NDYI、NREDI2、NREDI3、WRI、GCVI
GS	NREDI3、OSAVI、B6、NREDI2、NDYI
HB	NREDI3、NREDI2、OSAVI、NDVI、NREDI1
HN	OSAVI、NREDI2、EVI、NREDI1、NDVI
HuB	NREDI3、LSWI、GCVI、GNDVI、NDWI
JS	NREDI3、EVI、NREDI1、NREDI2、WRI
NM	NREDI3、NDYI、OSAVI、NREDI2、B6
NX	NREDI3、OSAVI、B6、NREDI2、NDVI
QH	NREDI3、NREDI2、WRI、GNDVI、NDWI
SAX	NREDI3、NREDI2、NREDI1、OSAVI、NDVI
SC	NREDI3、NDYI、OSAVI、NREDI2、NREDI1
SD	SWI、NREDI3、OSAVI、GNDVI、NDVI
SX	SWI、OSAVI、NREDI2、EVI、NDVI
XJ	EVI、B8A、B7、B8、NREDI3
ZJ	RVI、NREDI3、SWI、LSWI、NREDI2

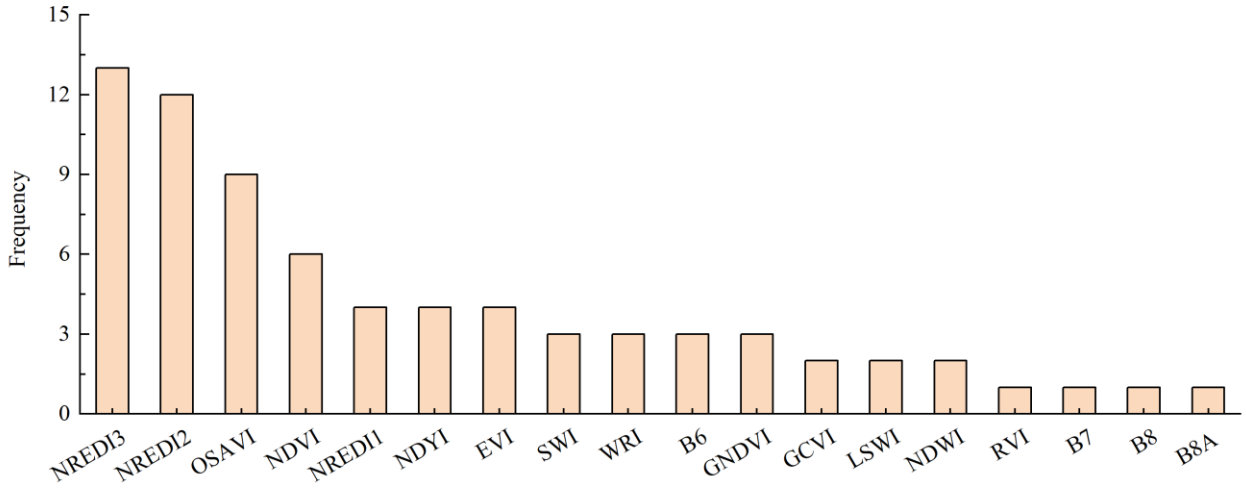

Figure S7: Frequency used for different spectral features.

References

Fernández-Manso, A., Fernández-Manso, O., and Quintano, C.: SENTINEL-2A red-edge spectral indices suitability for discriminating burn severity, Int. J. Appl. Earth Obs. Geoinf., 50, 170-175, https://doi.org/10.1016/j.jag.2016.03.005, 2016.

Gao, B.-C.: NDWI—A normalized difference water index for remote sensing of vegetation liquid water from space, Remote Sens. Environ., 58, 257-266, https://doi.org/10.1016/S0034-4257(96)00067-3, 1996.

Gitelson, A. and Merzlyak, M. N.: Quantitative estimation of chlorophyll-a using reflectance spectra: Experiments with autumn chestnut and maple leaves, Journal of Photochemistry Photobiology B: Biology, 22, 247-252, https://doi.org/10.1016/1011-1344(93)06963-4, 1994.

Gitelson, A. A., Kaufman, Y. J., and Merzlyak, M. N.: Use of a green channel in remote sensing of global vegetation from EOS-MODIS, Remote Sens. Environ., 58, 289-298, https://doi.org/10.1016/S0034-4257(96)00072-7, 1996.

Gitelson, A. A., Viña, A., Arkebauer, T. J., Rundquist, D. C., Keydan, G., and Leavitt, B.: Remote estimation of leaf area index and green leaf biomass in maize canopies, Geophys. Res. Lett., 30, https://doi.org/10.1029/2002GL016450, 2003.

Huete, A., Didan, K., Miura, T., Rodriguez, E. P., Gao, X., and Ferreira, L. G.: Overview of the radiometric and biophysical performance of the MODIS vegetation indices, Remote Sens. Environ., 83, 195-213, https://doi.org/10.1016/S0034-4257(02)00096-2, 2002.

Jordan, C. F.: Derivation of leaf-area index from quality of light on the forest floor, Ecology, 50, 663-666, https://doi.org/10.2307/1936256, 1969.

Li, S., Wang, S., Zheng, Z., Wan, D., and Feng, J.: A new algorithm for water information extraction from high resolution remote sensing imagery, 2016 IEEE International Conference on Image Processing (ICIP), 4359-4363, https://doi.org/10.1109/ICIP.2016.7533183,

Rondeaux, G., Steven, M., and Baret, F.: Optimization of soil-adjusted vegetation indices, Remote Sens. Environ., 55, 95-107, https://doi.org/10.1016/0034-4257(95)00186-7, 1996.

Sulik, J. J. and Long, D. S.: Spectral considerations for modeling yield of canola, Remote Sens. Environ., 184, 161-174, https://doi.org/10.1016/j.rse.2016.06.016, 2016.

Xiao, X., Boles, S., Frolking, S., Li, C., Babu, J. Y., Salas, W., and Moore III, B.: Mapping paddy rice agriculture in South and Southeast Asia using multi-temporal MODIS images, Remote Sens. Environ., 100, 95-113, https://doi.org/10.1016/j.rse.2005.10.004, 2006.

Zhang, H., Liu, W., and Zhang, L.: Seamless and automated rapeseed mapping for large cloudy regions using time-series optical satellite imagery, ISPRS J. Photogramm. Remote Sens., 184, 45-62, https://doi.org/10.1016/j.isprsjprs.2021.12.001, 2022.